Azimuthal distortion of the seismic focal sphere: application to earthquakes in subduction

Julie Perrot [a,*], Anne Deschamps [a], Veronique Farra [b], Jean Virieux [a]

[a] Institut de Géodynamique, Nice–Sophia Antipolis, France
[b] Département de Sismologie, Institut de Physique du Globe de Paris, Tour 14–24, place Jussieu, 75005 Paris, France

Abstract

New broadband seismographs enable us to analyse in more detail mantle waves perturbed by the complexity of the medium around the source. We propose to apply ray tracing for complex media around the source and more efficient ray tracing for a spherically symmetric Earth through the mantle up to the stations. We show on synthetic examples that the complexity around the source may indeed modify considerably the seismograms. We analyse theoretical teleseismic waveforms and relate modulation of the amplitude to the medium's structure around the source. For the example of the Romanian earthquake of 30 May 1990, we analyse three seismograms which were not modelled correctly with a spherically symmetric Earth model. By adding some near-surface interfaces, we were able to improve the fit between observed and computed seismograms. The deduced hypothetical model, which may not be the only possible model, is in agreement with proposed published models in the area.

1. Introduction

Seismic data accumulations as well as the improvement in the quality of seismic instruments allow seismologists to analyse many converted phases arriving inside the time window of the long-period teleseismic body waveforms used for source studies. When these phases are found at different stations, one can suspect that they are generated inside the source area. The medium around the seismic source always has a complex tectonic structure associated with the occurrence of earthquakes. This is especially true for subduction earthquakes. The analysis of the source rup-

ture must take into account these converted phases generated inside the source area. Wiens (1989) has analysed the effects of seafloor bathymetry and/or a sediment layer, and found, using ray tracing, that the dip of the seafloor is an important parameter for generating complex waveforms for P waves. He stated that realistic topography should be taken into account when high-order multiples are considered. The effect of realistic seafloor has also been underlined by Okamoto and Miyatake (1989) using a finite difference propagation inside the source area.

We propose in this paper a method to incorporate a two-dimensional (2D) complex propagation around the source in seismic source studies and to retain the ease of standard ray tracing tools for the mantle propagation. After a description of

---

* Corresponding author.

the proposed hybrid ray method, we test this method on synthetic data and apply it to the Romanian earthquake of 30 May 1990.

2. Ray tracing strategy

Ray tracing is the basic tool for wave propagation through the mantle. The associated high-frequency approximation is an adequate approximation for synthesizing teleseismic body waveforms. Although other techniques such as finite difference codes (Okamoto and Miyatake, 1989) can be used inside the source area, it seems important for interpretation analysis to retain ray tracing as the wave propagation tool. Contributions of a specified area of the medium to seismograms can be analysed easily with ray theory, whereas tracking the source of wave energy with finite difference codes is always more difficult. Moreover, the same approximation, the ray approximation, is used in a consistent way along the whole propagation path.

Two basic strategies can be proposed: the first is to use a spherical coordinate system for ray tracing both in the complex medium around the source and in a spherically symmetric Earth as soon as the ray enters the mantle. Because the

medium around the source is rather small (100 km by 100 km is a typical size), we have preferred another strategy, which is similar to that proposed also by Kendall and Thomson (1993) for an anisotropic 3D medium. Waves propagate in a 2D medium described by a cartesian coordinate system while the ray is near the source. Outside the complex medium we switch to a fast ray tracing in a spherically symmetric medium up to the station where synthetic seismograms are computed. Standard models such as PREM (Preliminary Reference Earth Model; Dziewonski and Anderson, 1981) are used for the spherically symmetric model inside which the fast analytical ray tracing proposed by Červený and Janský (1983) is performed.

Care must be taken to transform wavefront information properly from the local cartesian model to the global Earth model. The connection between the two ray tracers will be through a plane which will be called the hybrid plane (Fig. 1). This hybrid plane corresponds to a horizontal plane for the cartesian coordinate system and to a constant-radius surface for the global coordinate system. Whatever the velocity around the source, the velocity must be the same everywhere on the hybrid plane associated with the velocity specified in the 1D model. At the hybrid plane,

source

Numerical ray tracing
in a complex 2-D media

Representation of the
media by b-splines

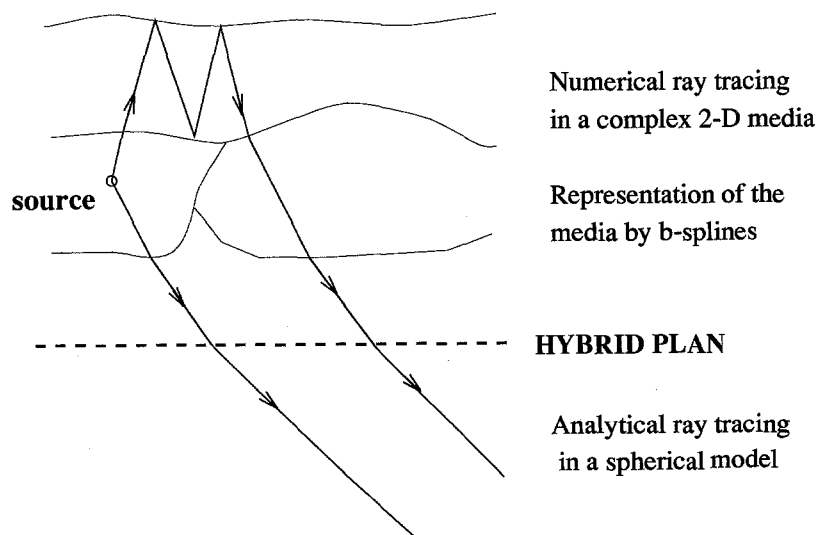HYBRID PLAN

Analytical ray tracing
in a spherical model

Fig. 1. Schematic propagation in the complex medium above the hybrid plane and in the homogeneous medium below.

we convert from local cartesian coordinates to global cartesian and spherical coordinates the various quantities needed for ray tracing such as the slowness vector or the paraxial vectors. Initial conditions on the hybrid plane are different from point source conditions usually required for teleseismic ray tracing.

The kinematic and paraxial ray tracing is based on the cartesian integration of ray tracing equations using a very specific sampling parameter τ defined by $ds = u(q)\,d\tau$ along the ray as suggested by Chapman (1985) and applied by Virieux et al. (1988) to the earthquake location problem. Using the Hamiltonian proposed by Burridge (1976),

$$H(\tau, q, p) = \tfrac{1}{2}\left[p^2 - u^2(q)\right] \tag{1}$$

for the eikonal equation, we obtain the ray tracing equations for the slowness vector p and the position vector q,

$$dq = \nabla_p H\,d\tau = p\,d\tau$$

$$dp = -\nabla_q H\,d\tau = \tfrac{1}{2}\nabla_q u^2\,d\tau \tag{2}$$

and the travel time T,

$$dT = u^2(q)\,d\tau \tag{3}$$

$u^2(q)$ is the square of slowness at q interpolated with b-splines in the 2D cartesian coordinate system. Interfaces are also described with b-splines and can have any a priori shape (Virieux and Farra, 1991).

The paraxial ray tracing is used to estimate the amplitude of a ray and, consequently, the seismogram. With the Hamiltonian perturbation technique used by Farra and Madariaga (1987), the ray tube is constructed with nearby trajectories obtained by perturbation of the central ray. This linearization gives us a stable estimation of the ray tube, as the variation of the media seen by the central ray will change the trajectory of the nearby one. A nearby trajectory, called the paraxial trajectory, is defined by

$$q(\tau) = q_0(\tau) + \delta q(\tau)$$

$$p(\tau) = p_0(\tau) + \delta p(\tau) \tag{4}$$

with the position $q_0(\tau)$ and slowness vector $p_0(\tau)$ of the central ray. The perturbations of the position vector q and slowness vector p verify the paraxial equations deduced by linearization of (2)

$$\begin{bmatrix} d\delta q/d\tau \\ d\delta q/d\tau \end{bmatrix} = \begin{bmatrix} \nabla_q\nabla_p H & \nabla_q^2 H \\ -\nabla_q^2 H & -\nabla_p\nabla_q H \end{bmatrix} \begin{bmatrix} \delta q \\ \delta p \end{bmatrix} \tag{5}$$

where H and its derivatives are computed on the central ray at τ.

The solution of this system can be solved by propagator techniques (Aki and Richards, 1980). For an initial vector $(\delta q(\tau_0), \delta p(\tau_0))$, the paraxial vector at the sampling parameter τ is given with the help of the propagator through

$$\begin{bmatrix} \delta q(\tau) \\ \delta p(\tau) \end{bmatrix} = P(\tau, \tau_0) \begin{bmatrix} \delta q(\tau_0) \\ \delta p(\tau_0) \end{bmatrix} \tag{6}$$

with the definition of the propagator as partial derivatives with respect to initial position (x_0, z_0) and initial slowness (px_0, pz_0)

$$P = \begin{pmatrix} \partial x/\partial x_0 & \partial x/\partial z_0 & \partial x/\partial px_0 & \partial x/\partial pz_0 \\ \partial z/\partial x_0 & \partial z/\partial z_0 & \partial z/\partial px_0 & \partial z/\partial pz_0 \\ \partial px/\partial x_0 & \partial px/\partial z_0 & \partial px/\partial px_0 & \partial px/\partial pz_0 \\ \partial pz/\partial x_0 & \partial pz/\partial z_0 & \partial pz/\partial px_0 & \partial pz/\partial pz_0 \end{pmatrix}$$

$$= \begin{pmatrix} \delta qx_1 & \delta qx_2 & \delta qx_3 & \delta qx_4 \\ \delta qz_1 & \delta qz_2 & \delta qz_3 & \delta qz_4 \\ \delta px_1 & \delta px_2 & \delta px_3 & \delta px_4 \\ \delta pz_1 & \delta pz_2 & \delta pz_3 & \delta pz_4 \end{pmatrix} \tag{7}$$

The propagator P defined as partial derivatives of position and slowness vector with respect to different initial perturbations is a 4×4 matrix for a 2D cartesian coordinate system. The subscripts 1 and 2 denote the two selected elementary trajectories for plane wave source conditions, i.e. $(1,0,0,0)^t$ and $(0,1,0,0)^t$, and the subscripts 3 and 4 denotes the two selected elementary trajectories for point source conditions $(0,0,1,0)^t$ and $(0,0,0,1)^t$ (see Červený, 1985), where we give the initial paraxial vector using the transpose notation t.

An additional condition is required if one wants the paraxial trajectory to describe a paraxial ray. The vector $(\delta q(\tau), \delta p(\tau))$ should satisfy an additional condition derived from the perturbation of the eikonal equation $H = 0$. The follow-

ing perturbation of the Hamiltonian should be satisfied by the paraxial vector:

$$\delta H = p_0 \delta p - \tfrac{1}{2} \nabla_q u_0^2 \delta q = 0 \qquad (8)$$

As δH is constant along a paraxial ray, it is sufficient to enforce $\delta H = 0$ at the source to satisfy this condition anywhere.

As an example, the point source condition is such that $\delta q(\tau_0) = 0$ and $\delta p(\tau_0) \perp p_0$, which can be obtained by linear combination of the two elementary point source trajectories. The plane source condition are given by $\delta q(\tau = 0) \perp \nabla_q u^2$ and $\delta p(\tau = 0) = 0$. The selection of the initial δq depends on the velocity variation at the source and can be taken when the seismogram at the station is going to be constructed. Therefore, WKBJ initial conditions (Chapman, 1985) as well as Červený (1985) initial conditions can be specified once the ray reaches the station by combining differently the four elementary trajectories. Whereas the propagator for paraxial trajectories is a 4×4 matrix, the propagator for paraxial rays is only a 2×2 matrix.

At the hybrid plane, we resume the propagation in the cartesian coordinate system. We save quantities necessary for the kinematic ray tracing (the travel time Θx, the distance Δ_x and the
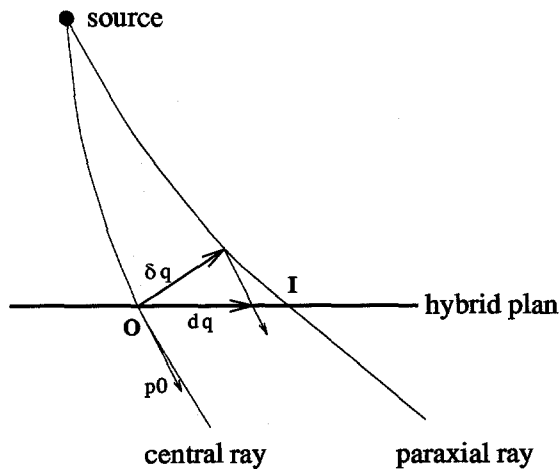

Fig. 2. Geometry of the interaction of a ray and one of its paraxial rays with the hybrid plane. The central ray intersects s at point O with the slowness vector $p0$ and the paraxial vector at I. At the hybrid plane, we transformed the paraxial vector δq and δp into dq and dp.

slowness vector p_x) as well as quantities necessary for the paraxial ray tracing contained in the propagator P. The conditions for switching from one ray tracer to the other are the continuity of the travel time, the distance and the slowness vector, as well as the continuity of the projection of the propagator P through the hybrid plane. To verify the last continuity condition, the propagator P is projected on the hybrid plane by a linear transformation with the matrix Π of Farra et al. (1989). Because the velocity is continuous through the hybrid plane, the second matrix T, found also in Farra et al. (1989) to ensure the continuity of the ray tube through the hybrid plane, is the identity. We obtained the perturbed paraxial vector on the the hybrid plane (dq, dp) for a paraxial ray at point I with respect to the central ray at the intersection point O, from the perturbation vector $(\delta q, \delta p)$ (Fig. 2):

$$\begin{bmatrix} dq \\ dp \end{bmatrix} = \Pi \begin{bmatrix} \delta q \\ \delta p \end{bmatrix} \qquad (9)$$

Thus, the projected matrix P_t becomes the representation of the perturbation of the position and slowness paraxial rays on the hybrid plane. The partial derivatives are now taken in such a way that z is kept constant, which allows us to write

$$P_t = \begin{pmatrix} dqx_1 & dqx_2 & dqx_3 & dqx_4 \\ 0 & 0 & 0 & 0 \\ dpx_1 & dpx_2 & dpx_3 & dpx_4 \\ dpz_1 & dpz_2 & dpz_3 & dpz_4 \end{pmatrix}. \qquad (10)$$

We are interested in the reduced propagator obtained from paraxial rays and not from paraxial trajectories. Simple linear combinations of the paraxial trajectories to satisfy (8) give us the projection of the cartesian propagator for paraxial rays P_x, which is a 2×2 matrix and which is often written, following Červený (1985),

$$P_x = \begin{pmatrix} Q_1 & Q_2 \\ P_1 & P_2 \end{pmatrix} \qquad (11)$$

where Q_1, Q_2, P_1, P_2 are submatrices containing elementary trajectories for point and plane wave source conditions. The propagation continues on the spherically symmetric medium toward the station as shown in Fig. 3. Ray integrals are com-
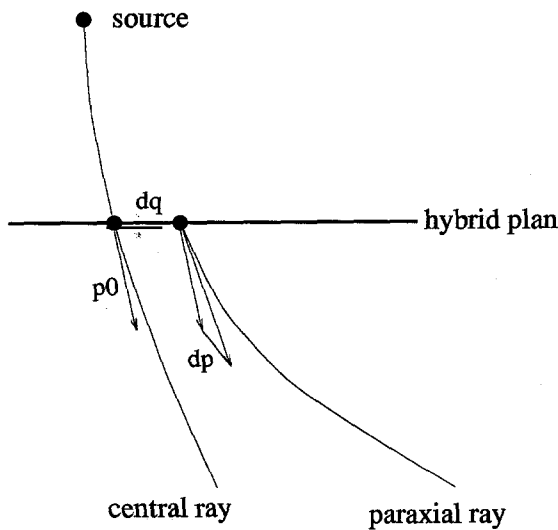
Fig. 3. The spherical propagation begins at the hybrid plane with new plane source conditions for the paraxial ray. Finally, the whole propagator will be the product of the matrix P_s with the matrix of the cartesian propagator P_x.

puted using a particular interpolation of the radial variation of the velocity described by Červený and Janský (1983). Estimation of integrals of the travel time Θ_s and the distance Δ_s is fast and stable. Moreover, derivatives of ray integrals with respect to the ray parameter can be computed by simple analytical quadrature and allow us to estimate the partial derivative $\partial\Theta/\partial p_r$ with p_r the ray parameter and the associated global cartesian geometrical spreading Q_{2r}. The corresponding propagator equals

$$P_s = \begin{pmatrix} 1 & Q_{2r} \\ 0 & 1 \end{pmatrix} \tag{12}$$

The first column gives the horizontal perturbation of position and slowness for initial WKBJ conditions. This solution is simply a vertically varying velocity. The second column gives the more complex solution for initial point source conditions where only perturbation of the slowness parameter is kept constant. We must combine these solutions with starting conditions on the hybrid plane given by (11). In other words, we must multiply this cartesian propagator P_s on a spherically symmetric Earth by the local cartesian propagator P_x.

The physical quantities of the propagation at the station are: the travel time, $\Theta = \Theta_s + \Theta_x$; the distance, $\Delta = \Delta_s + \Delta_x$; the propagator, $P = P_s \times P_x$. With these quantities of kinematic and paraxial ray tracing, we estimate the terms of the cartesian Green function G at the station x from a source at the origin as the 2D geometrical spreading J_{2d}, the so-called kmah index k and the take-off angle Φ_s. To construct the Green function, we will use the approximation in a 3D medium with an invariance along an axis direction called the 2.5D approximation. For that we need to extend the 2D geometrical spreading in a 2.5D geometry (Lambaré et al., 1992):

$$J_{2.5d} = J_{2d}(\tau/v_0) \tag{13}$$

with v_0 the velocity computed at the source and τ computed at the receiver. Following Langston and Helmberger (1975), the Green function will be

$$G_i(x,t)$$

$$= \mathrm{Re}\left[R_i C V \sqrt{\left(\frac{\rho_0 v_0}{\rho v}\right)}^{1/2} \frac{e^{i\pi k/2}}{\sqrt{|J_{2.5d}|}} D(t - T) \right] \tag{14}$$

with $D(t) = \delta(t) - (i/\pi t)$, where $\delta(t)$ is the dirac function. The Green function is decomposed into three elementary functions according to the vertical radiation patterns R_i, which depend only on ray tracing parameters: G_1 corresponds to a vertical strike-slip dislocation and G_2 to a vertical dip-slip dislocation in a north–south azimuth, and G_3 to a dislocation dipping at 45° in a N45° azimuth. The density ρ and the velocity v are computed at the station and ρ_0 is estimated at the source. The velocity is either the P-wave velocity or the S-wave velocity depending on the wave under consideration. The factor C is the product of refraction/reflection coefficients at the various interfaces met by the ray trajectory. The function V is the receiver function which includes the angle of the ray at the free surface at the station.

The radiation pattern is composed of the vertical radiation patterns R_i and the functions $A_i(\phi,\lambda,\delta)$, the radial component of the moment

tensor: $\Sigma_i R_i A_i(\phi,\lambda,\delta)$. All these parameters have been defined by Langston and Helmberger (1975) and discussed by Madariaga and Papadimitriou (1985); ϕ, λ and δ are respectively the strike, the rake and the dip angles of the seismic fault plane.

The convolution of the Green function with the source excitation and radiation pattern is obtained with the expression

$$G'(r,t) = \frac{\dot{M}_0}{4\pi\bar{\rho}_0} \sum_{i=1}^{3} G_i(x,t) A_i(\phi,\lambda,\delta) \qquad (15)$$

where $\dot{M}_0$ is the derivative of the seismic moment. Explicit expressions of these functions have been given by Madariaga and Papadimitriou (1985).

Finally, the synthetic seismogram $U(r,t)$ is the convolution of the Green function $G'(r,t)$ including the source time function with the instrumental response $I(r,t)$ and the mantle attenuation operator $Q(r,t)$:

$$U(r,t) = I(r,t) * Q(r,t) * G'(r,t) \qquad (16)$$

Careful checking has been performed for this ray tracing strategy. For a stratified medium, we obtained identical results using either the spherically symmetric ray tracing or the hybrid method. The cartesian medium should have a vertical variation of the velocity compatible with the spherically layered symmetry: a constant velocity for a spherical shell must be transformed in an exponential increase with depth for the cartesian layer (see Muller (1971) or Chapman (1987)).

3. Synthetic data

To illustrate a complex propagation around the source, we propose to study the propagation in a subduction zone and analyse the influence of the main shallow structures. The model (Fig. 4) is defined by a profile perpendicular to the subduction axis. We consider stations on both sides: the western part is the side of the subducted plate and the eastern part is the side of the overlying plate. The oceanic plate, a layer of 10 km thickness with constant P-wave velocity of 6.0 km s^{-1}, is gently dipping at a low angle of 1.5° towards the east, and the overlying plate has a constant velocity of 5.5 km s^{-1} and is dipping 4.0° towards the west. The slab is described by a bending of the oceanic crust, occurring just below the coastline, until it reaches a slope of 50°. The sea depth varies between 3 and 7 km in the studied zones and is great enough to allow a good separation of the reflected phases.

Depending on the position of the event, the influence of various parts of the structure can be seen on the seismograms, which are calculated for epicentral distances ranging from 30° to 90° in the east–west model direction. We use eight points per second as the sampling rate in the Green function calculation and, as this study is focused on water reflections, we do not include sP phases. We choose a dip-slip event at 13 km depth and vary its horizontal position with respect to the structure. Source duration is short (4
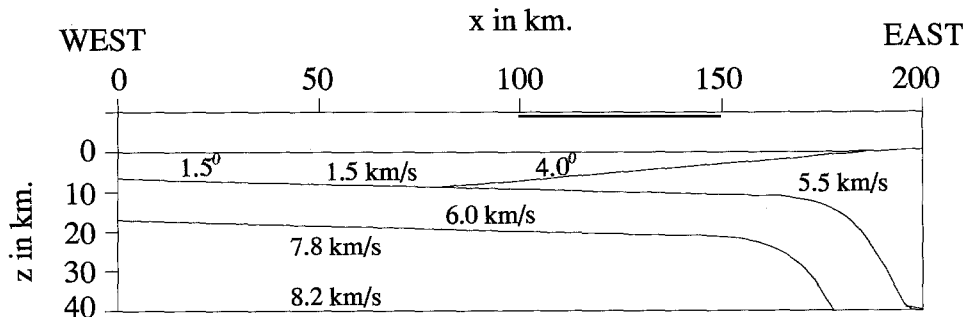

Fig. 4. The cartesian velocity model used in our synthetic testing is defined as a box of 150 km depth and 200 km width. The hybrid plane is fixed at 150 km. The 1.5° dipping interface is the oceanic seafloor, and the 4.0° dipping interface represents the continental margin. The velocities are given for P waves. (Note the water layer of velocity 1.5 km s^{-1}). Constant-velocity layers describe the subducted plate and the overlying plate, and a velocity gradient is used in the lithosphere.

s) and the hypothetical instrument has the broadband response of the COL VHZ channel, which is almost flat in velocity above 10 Hz.

3.1. Effect of water layer

In a first step, we suppose the seismic event is far from the trench, where the local model can be represented in a spherically symmetric Earth model using a layered medium with a water depth of 7 km and an oceanic crust of 10 km. We particularly analyse water multiples. In Fig. 5 are presented the Green functions corresponding to the three elementary mechanisms (from Eq. (14)) at four distances and in two opposite directions (east and west). The small time delay (less than 3 s) between pP, reflected at the seafloor, and the

P phase is controlled by the depth of the event and the P-wave velocity in oceanic crust. Multiples from the water layer arrive 15 s after the P phase (this delay is controlled by the water depth). The number of reflections are limited at three in these synthetic examples but the decrease of amplitude is regular, controlled only by the product of the two reflection coefficients in the water layer. In fact, in this example, where the velocity contrast at the seafloor is large (from 1.5 km s^{-1} in the water to 6.0 km s^{-1} in the oceanic crust), amplitudes are significant until the fifth reflection in the water layer.

Fig. 6(b) shows synthetic waveforms computed for the selected focal mechanism. The amplitudes of the various observed phases are controlled by the take-off angle of the ray on the focal sphere
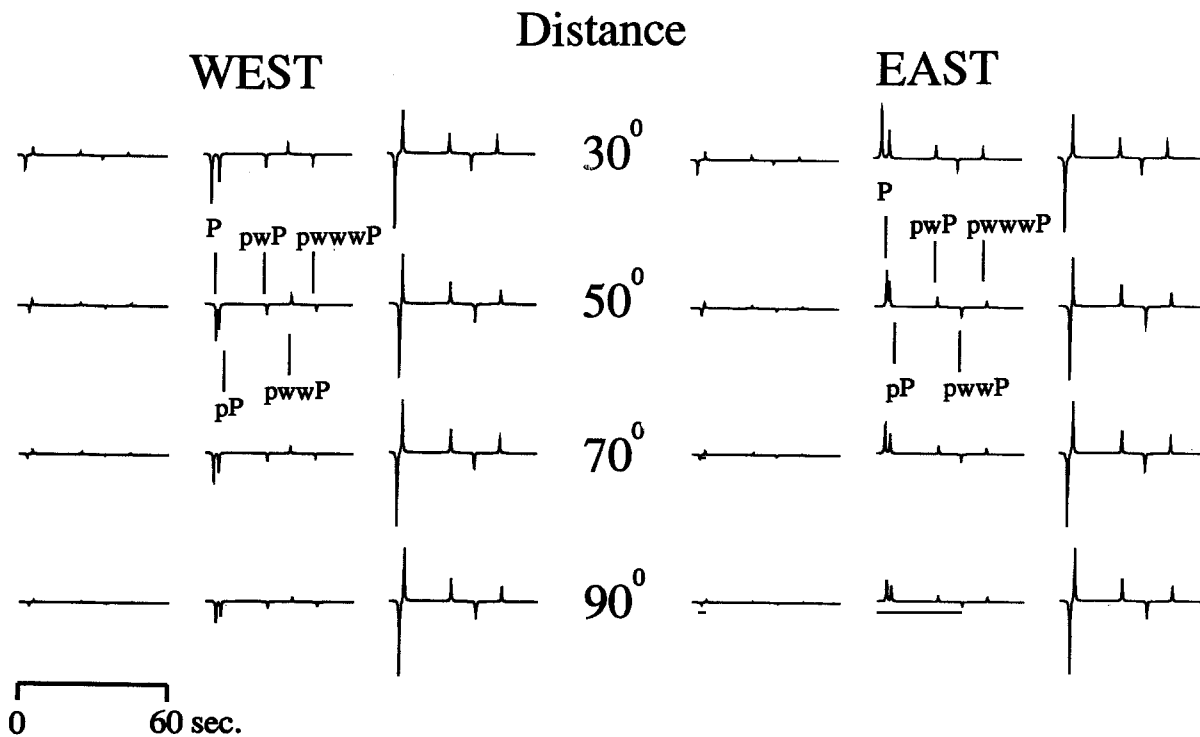

Fig. 5. The Green functions are calculated in a spherically symmetric Earth model, for a source at 13 km depth (7 km of water, 6 km of oceanic crust) at receiver distances of 30°, 50°, 70° and 90°. The elementary functions (from Eq. (16)) represent the three components of the moment tensor. The first main pulse is composed of the direct P wave and, 3 s later, the reflection pP at the seafloor. Reflections in the water layer (pwP, pwwP and pwwwP) could be distinguished 20 s later. Because of the symmetry of the elementary solutions, the phases have the same amplitude on both sides. We note the regular decay of the amplitude with the number of reflections in the water layer and the polarity change when an upward reflection at the sea bottom occurs, indicated by pwwP polarity.
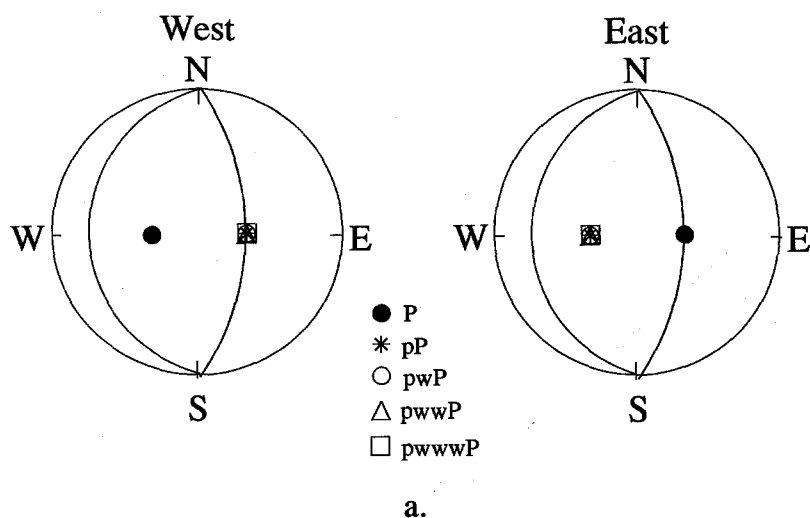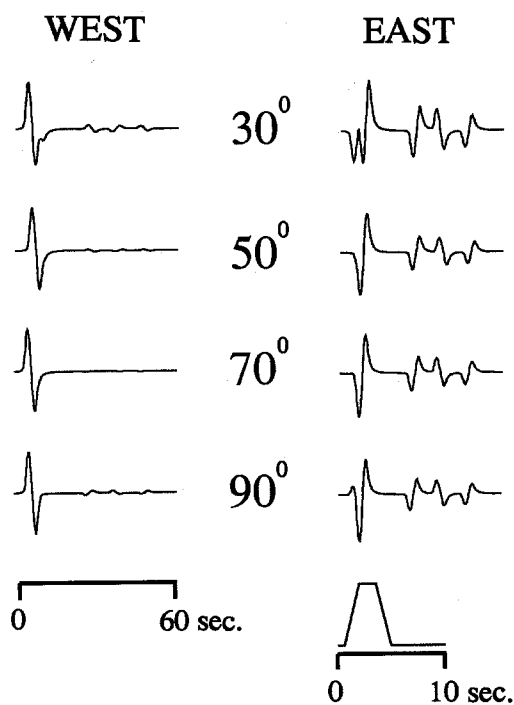
Fig. 6. (a) The thrust mechanism (strike 0°, dip 70°, slip 90°) used, shown on an equal area projection of the focal sphere. The take–off angles are plotted only for phases recorded at an epicentral distance of 50°. In the flat model, take-off angles of the reflected phases are all the same, on the nodal plane for rays going westward and in the high-amplitude domain of the radiation pattern for rays going eastward. (b) Synthetic seismograms computed with the model assuming horizontal interfaces, using Green functions of Fig. 5, for the thrust mechanism presented in (a) and convolved by a broadband instrumental response. The source is located at 13 km depth in the oceanic crust, and the time function is trapezoidal and 4 s long. The pP phase contributes to the main pulse and is not separated from the direct P phase except for seismograms at 30° distance; on the west side the P phase is dominant, whereas on the east side the pP phase is more important. There is almost no amplitude for the water reflections on the west side, whereas the large radiated amplitudes on the east side show clearly the slow decrease with number of water multiples.

represented in Fig. 6(a); in a flat velocity model the water multiple take-off angles and the pP phase take-off angle are equal. The first pulse of the synthetic seismogram is the summation of the P and pP phases, except for the 30° distance receiver where the time delay is longer than for the other receiver distances. The synthetic seismogram for a dip-slip event corresponds to a

particular case: it is dominated by the P phase in the western part and the pP phase in the eastern part as deduced from the position of the corresponding take-off angle on the P-wave radiation pattern. The same partition exists for multiples in the water layer: there is almost no energy on the western side (the take-off angles are near the nodal plane), whereas it could reach half that of
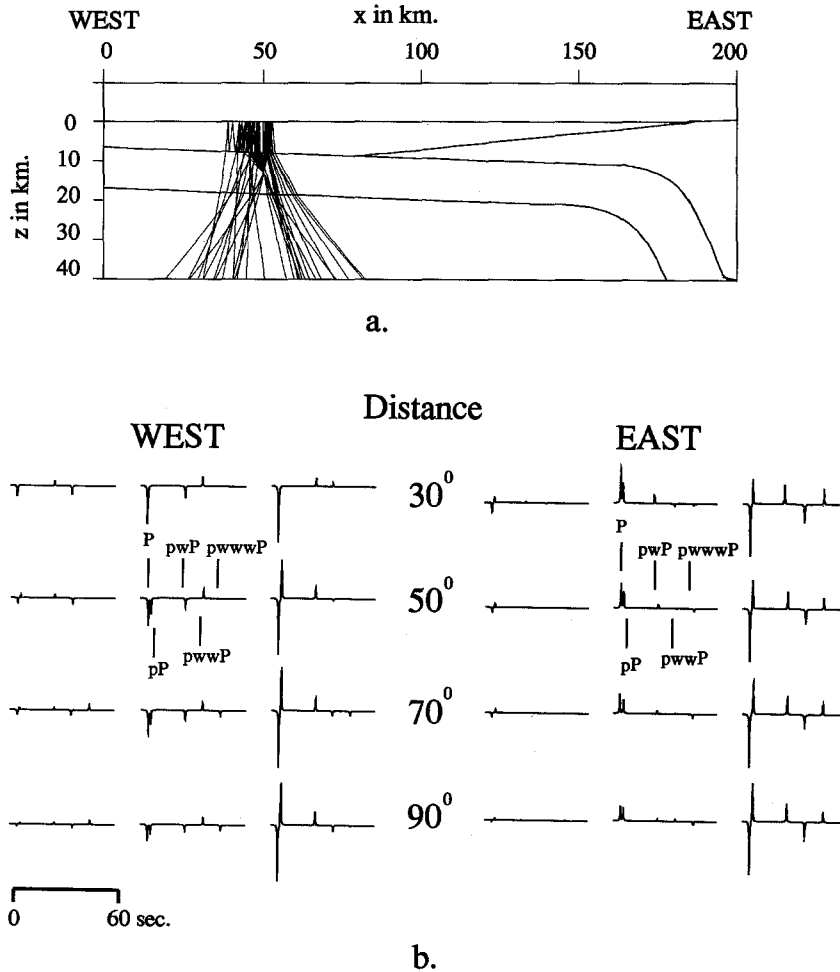

Fig. 7 (a) Ray tracing in a model with a 1.5° dipping seafloor. The source is located at 13 km depth in the oceanic crust. The depth of the water layer seen by the rays varies between 6 and 9 km above the oceanic crust. A large dispersion of the rays is observed on the west side; for the east side, reflected rays in the water layer are located just above the source. (b) Green functions corresponding to the ray tracing of (a) and in the same representation as in Fig. 5. The same phases as those obtained for the flat model (Fig. 5) are present in the signal. There are lower amplitudes for the reflected phases of the west side. Modelling of the third reflection in the water layer is not possible for the Green function of the 30° receiver distance on the west side.

West
N

East
N

W ⊣   ●   *○ △   □⊢ E

W ⊣   *○△□ ●   ⊢ E

● P
* pP
○ pwP
△ pwwP
□ pwwwP

S

S

a.

Distance

WEST   **EAST**

30⁰

50⁰

70⁰

90⁰
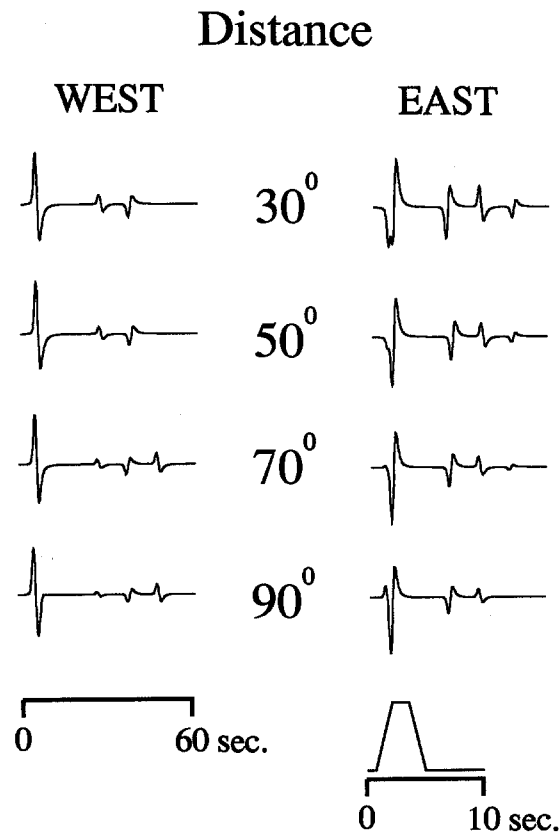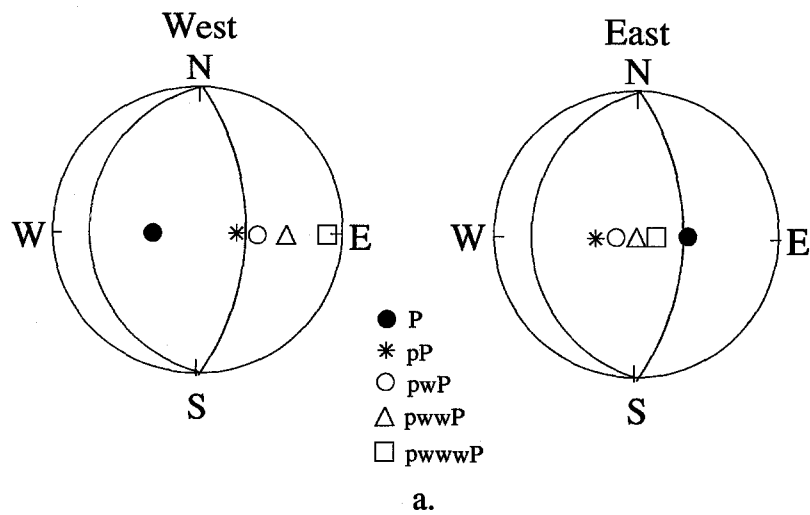
0   60 sec.

0   10 sec.

b.

Fig. 8. (a) Same as Fig. 6(a), but with take-off angles calculated from Fig. 7(a). On both sides the take-off angles are rotated to the east by the dipping seafloor when compared with the flat model. A greater folding of the focal sphere is observed for the west side: this results in a large shift of the take-off angle. (b) Synthetic seismograms computed for the 1.5° dipping seafloor model using the Green function of Fig. 7(b). The time delays of reflected phases are about the same as in the flat model. (Note the large amplitudes on the west side for the reflected phases in the water layer, increasing with the number of reflections for the distances 70° and 90° on the west side.)

the main pulse on the eastern side (the take-off angles correspond to the maximum amplitude of the radiation pattern).

3.2. Effect of dipping oceanic seafloor

We move the seismic event inside the oceanic crust towards the trench, at 50 km in our velocity model (Fig. 7(a)). The water depth above the source is the same as in the previous case; the effects of the dipping seafloor on multiple reflected phases in the water are the dominant factors.

In the Green functions presented in Fig. 7(b), we note mainly a variation of relative amplitudes of reflected phases, for the three types of mecha-
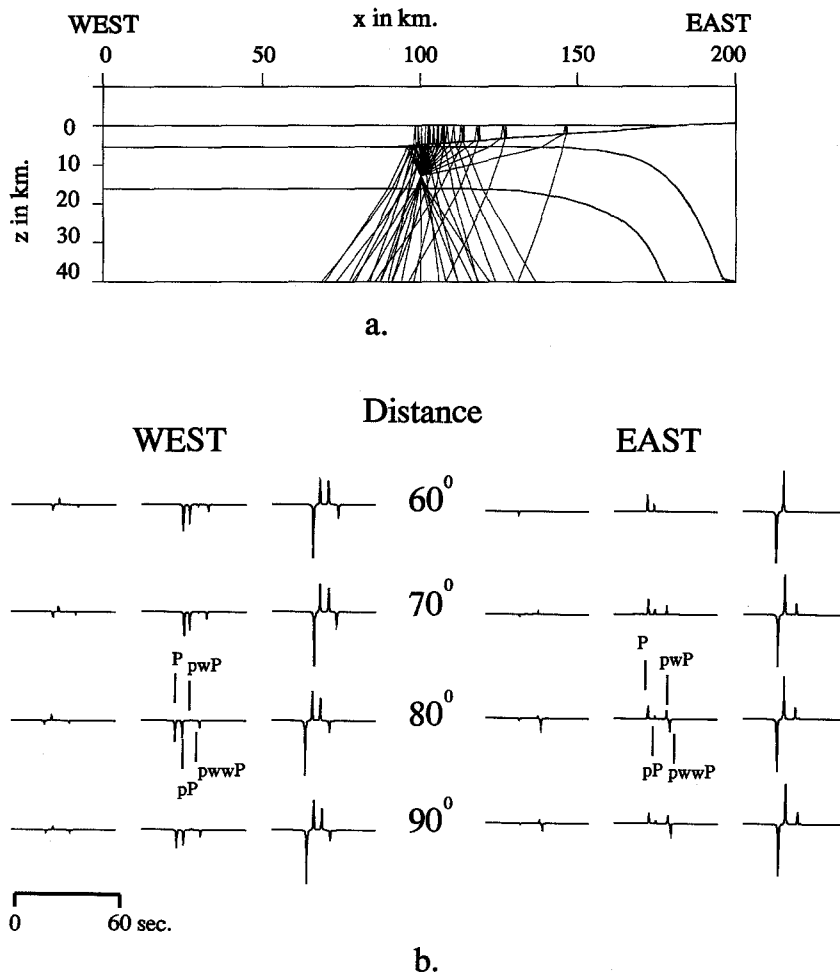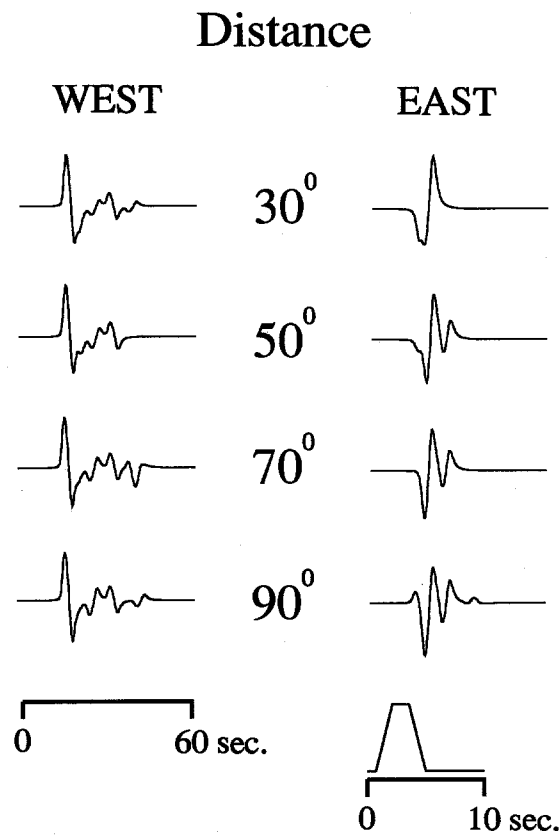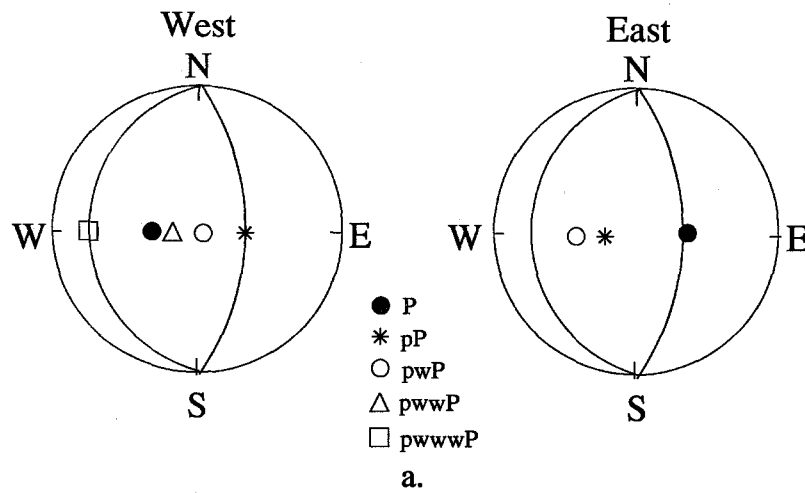

a.

b.

Fig. 9. (a) Ray tracing with the same model as for Fig. 7(a) but with a source located 50 km to the east at the same depth just above the continental margin. We observe a large dispersion of the water multiples on the east side owing to the 4° dip to the west of the continental margin. The water multiples with a take-off angle directed to the east at the source turn to the west after the second reflection in the water layer. (b) The Green functions corresponding to the ray tracing of (a) and in the same representation as in Fig. 5. Only three phases are present on the east side—P, pP and pwP. The Green functions of the west side show all the phases. The time delay of water multiples is shorter as the water layer is thinner (5 km) but the time delay of the pP phase is greater as its ray path is longer in the crust (8 km).

West   East

● P
✳ pP
○ pwP
△ pwwP
□ pwwwP

a.

Distance

WEST   EAST

30^0

50^0

70^0

90^0

0   60 sec.

0   10 sec.

b.

Fig. 10. (a) Same as Fig. 5(a) but with take-off angles calculated as in Fig. 9(a). We have a strong folding of the sphere for both sides, but in the opposite direction from that in the previous example, in the direction of the dip of the continental margin, to the west. (b) Synthetic seismograms computed using the Green functions of Fig. 9(b) for the crust above the continental slope with the same source parameters. The pP phase is always dominant on the east side but begins to be separated from the P wave as the water layer is thinner than in the previous examples (between 2 and 6 km). The reflected phases are also for this reason only 10 s after the main pulse for the east side. The reflected phases arrive 15 s after the main pulse on the west side. For this side, only the pP phase shows a high amplitude.

nisms and for west and east directions. There are also small differences in arrival times of the phases. As shown in Fig. 7(a), the dipping seafloor changes ray trajectories and therefore the associated reflection/refraction coefficients and geometrical spreading, as well as the radiated amplitude at the source (Fig. 7(b)). The variation of the take-off angle increases with the number of reflections on the dipping interface (Fig. 8(a)), and

it strongly modulates the amplitude of the reflected phases, as mentioned by Wiens (1987). In the western direction, the take-off angle increases and rotates from an almost nodal amplitude for the pP phase to a maximum amplitude for the pwwP phase for the focal solution that we selected. In the eastern direction, it decreases so that the amplitudes of the reflected phases decrease more strongly than in the flat model.
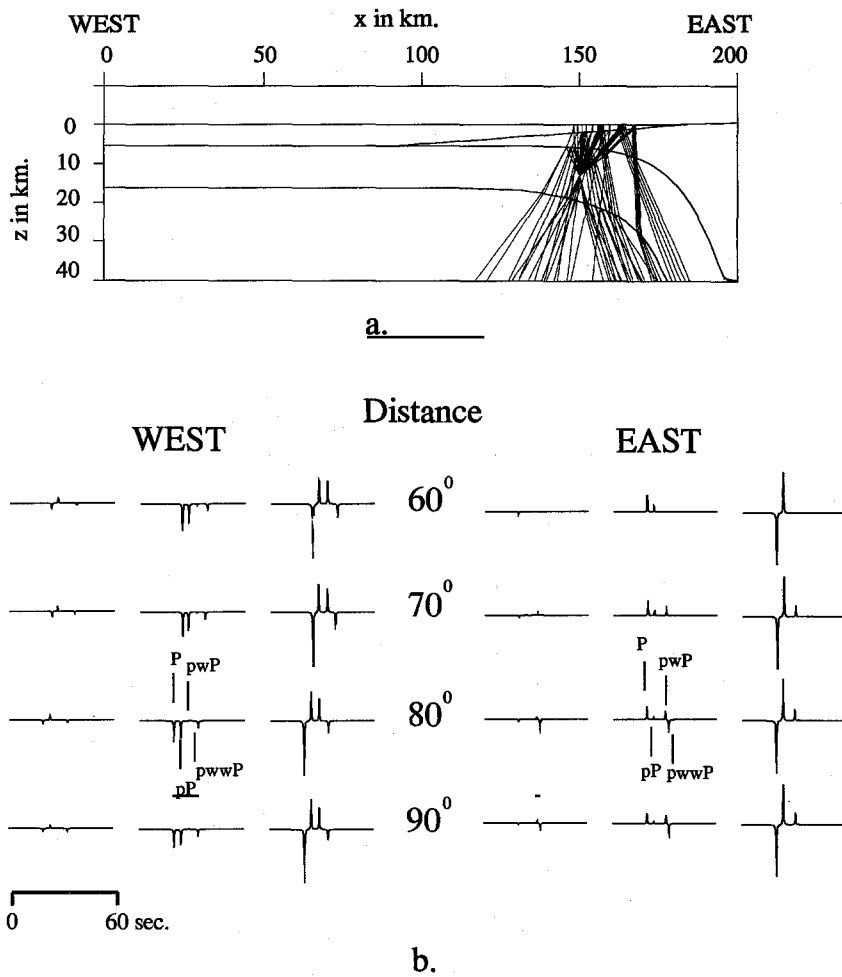

Fig. 11. (a) Ray tracing with the same model as in Fig. 7(a) but with a source located in the curved slab at the same depth, 13 km. The water depth varies between 1 and 3 km. (Note the variations of angles at the curved slab.) The path in the oceanic crust is longer than in the previous example. (b) The Green functions corresponding to the ray tracing of Fig. 9(a) and in the same representation as in Fig. 5, but for 60°, 70°, 80° and 90° receiver distance. The third reflection in the water layer is not possible at these distances. For the east side, no water multiple is recorded for the 60° distance and the pwwP phase is not present in the Green function for the 70° distance. The pwwP phase shows a higher amplitude than the pwP phase owing to the focusing of the rays crossing the curved slab.

The rays, transmitted in the water layer through the 1.5° dipping seafloor, have less vertical take-off angles than those computed in the flat model. Reported on the focal sphere, the take-off angles are shifted along the azimuth of the station in the direction of the dipping seafloor. This effect, which we call the azimuthal distortion of the focal sphere, is important and different for each phase.

The computed synthetic seismogram (Fig. 8(b)) shows the same characteristics as for the flat model. The first main pulse is dominated by the P direct phase on the western side and by the pP wave on the eastern side; changes are not detectable. The time delay of the water reflected phases is also nearly the same in the two models. However, relative amplitudes of the water reflections are strongly perturbed at some distances. For instance, we can observe an increase in the amplitude of the water multiples with the number of reflections at distances of 70° and 90° on the western side whereas on the opposite side the decrease is reinforced so that the third reflection disappears.

### 3.3. Effect of continental margin dipping westward

The third calculation is to show the effect of the presence of the subducting crust, dipping 4° to the west above the oceanic crust (which is kept flat for simplification). With the same characteristics as before, the source is located at 100 km in our model, in the horizontal plane where the subducting crust is about 0.5 km thick (Fig. 9(a)). The main features of the Green functions (Fig. 9(b)) are associated with the large westward-dipping seafloor interface. Phases created at the ocean–continent interface and multiple reflections inside the continental crust are not considered because of their negligible amplitudes. The time delays of the water layer multiples are shorter than in the previous examples, and the sea layer is thinner, varying between 2 and 5 km. Time delays of the pP phase, particularly on the eastern side, are greater as the pP paths in the two crusts are longer, and therefore P and pP phases can be distinguished on some synthetic seismograms (Fig. 10(b)).

The main part of the energy is redirected by dipping of the continental margin to the western side (Fig. 9(a)); the rotation of the take-off angles, presented in Fig. 10(a), is important for both sides. This feature, associated with the strong contrast of velocity (1.5 km s^{-1} for the water and 5.5 km s^{-1} for the continental crust), does not allow the transmission of the second pwwP and the third pwwwP reflection in the water layer toward eastern sites, where only P, pP and pwP phases are needed to construct the Green functions (Fig. 9(b)). On the synthetic waveform (Fig. 10(b)), the main pulse is similar to that calculated in the previous examples; there is only a small enlargement owing to the mean relative position of the source beneath the seafloor. A strong variation of the amplitudes of the multiple reflected waves is observed between east and west directions as well as with epicentral distance.

3.4. Effect of oceanic crust curvature and presence of a slab

In the last synthetic example, we are interested in the influence of the slab structure. The source is at 150 km in our model definition, still inside the oceanic crust and where the curvature of the plate is important (Fig. 11(a)). The sea layer and crustal thickness above the source are respectively 2 km and 11 km. The mean time delay between the P and pP phases is about 5 s, and multiple water reflections arrive faster after the P phase than in the previous calculations. The effect on the ray paths of the curvature of the interface between the two crusts cancels the effect of the slope of the continental margin: rays are focused towards the east (Fig. 11(a)). Neither to east nor to west did direct P waves arrive at epicentral distances between 30° and 50°; they cannot be transmitted through the interfaces of the slab. Therefore we choose to represent Green functions and synthetic seismograms at distances between 60° and 90°. With this distance range, it is impossible to record the reflected phases which propagate in the slab.

The first reflection in the water layer, pwP, is not present in the Green function (Fig. 11(b)) at receiver distance 60° east, as it is not transmitted

a.
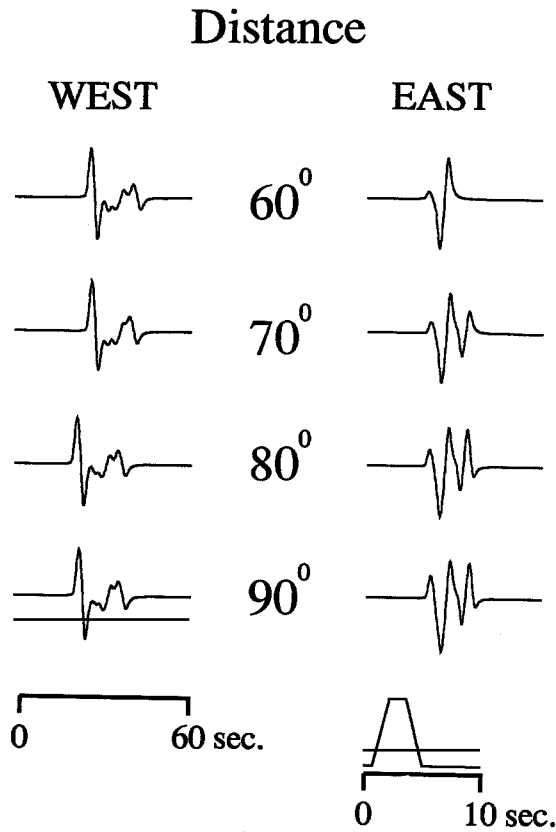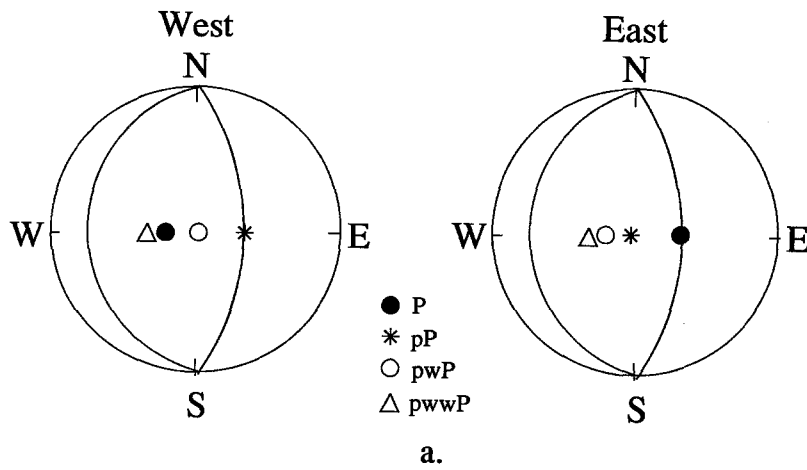
Distance

b.

Fig. 12. (a) Same as Fig. 5(a) but with take-off angles calculated as in Fig. 11(a) and for the 80° receiver distance. We have a distortion of the sphere to the east for the reflected phases, as in the previous example. (b) Synthetic seismograms computed using the Green functions of Fig. 11(b). For the east side, the reflected phases show amplitudes even higher than those of the pP phase for the 80° and 90° distance on the east side. For the west side, the main pulse is composed of the P wave, followed 15 s later by the pwwP phase.

through the curved slab. The time delay of the pwP phase on the east side is longer by 2 s than the time delay of the pwP phase on the west side because the rays have travelled further in the crust. The amplitude of this phase is lower in the Green function of the east side but the drift of the take-off angle (Fig. 12(a)) is decreased compared with the previous example, owing to the competitive effects of the curved slab. Therefore, the amplitude of the pP phase is increased, as its position on the radiation pattern is now in the maximum of amplitude for the 80° and 90° east receiver distance (Fig. 12(b)).

The pwwP phase for 60° and 70° east receiver distance is not present in the Green function (Fig. 11(b)), as it cannot cross the curved slab. The time delay for this phase compared with the pwP phase at 80° and 90° receiver distance varies on both sides: the pwwP phase arrives 2 s earlier than the pwP phase on the east side and 5 s earlier on the west side. This short time delay on the east side results from a ray path in the thinner part of the water layer for the pwwP phase. Its amplitude in the Green function is greater on both sides than those obtained in the previous example; we attribute this effect to ray focusing through the curved slab as these rays cross the curved slab. The large contrast of velocity associated with the strong dip of the continental margin did not allow the third reflection in the water layer on both sides to be transmitted downward.

On seismograms of the west side, the main pulse is the P wave, whereas the pP phase has a rather low amplitude because its take-off angle is on a nodal fault plane. The signal which arrives just after the main pulse comes from the pwwP phase, whose take-off angle on the focal sphere is located in the high-energy part of the radiation pattern.

We have analysed two types of effects of major near-surface structures of a subduction zone from a shallow gently dipping seafloor to a deeper curved slab. The first effects are observed in the Green function; we called these the propagation effects, as the propagation in a complex 2D medium provides variation in the geometrical spreading and the reflection/transmission coeffi-

cients. From the dipping seafloor to the dipping continental margin, the strong contrast in velocity (1.5 km s^{-1} compared with 6.0 km s^{-1}) associated with the dipping interfaces ($1.5°$ and $4.0°$) reinforces the reflection/transmission coefficients. The second effect is the variation of the take-off angle position on the focal sphere: we called this the azimuthal distortion of the focal sphere. It results from the convolution of the Green function with the radiation pattern; therefore it is completely dependent on the focal mechanism. Synthetic seismogram examples show that the shift of the take-off angles is in the direction of the dipping interfaces. For the curved slab, this shift is in the direction of the plunging slab. The distortion of the focal sphere may amplify or cancel the propagation effects; for this reason, its contribution is the most important effect. This distortion effect on the focal sphere occurs in the azimuth of the station such as we propagate in a 2D subduction zone model. With a 3D model, this effect will not be restricted in the azimuth of the station.

4. The Romanian earthquake of 1990

A magnitude 6.7 event occurred in the Vrancea area on 30 May 1990, at a depth of 90 km, and has been recorded on broadband stations. On records at stations in the southeastern quadrant, for three examples (HYB, AGD and RER) relative amplitudes of P, pP and sP phases cannot be modelled by any focal mechanism radiating in a spherical Earth. The intermediate depth of the event and the relatively small magnitude allow a clear observation of the three phases, which are well separated in time. We verify also that no other arrivals such as PcP could significantly perturb surface reflections. A similar observation was also reported by Monfret et al. (1990) for the record at RER of the 1986 event which occurred in the same area, but at a depth of 140 km (Tavera, 1991). As the same anomalies were found at the same station for these two events, the propagation around the source must explain the observed anomalies. The amplitude effects are

large; therefore heterogeneities must change significantly the ray parameters, corresponding to a large change of P and pP amplitudes in the radiation pattern.

The focal mechanism of the 1990 earthquake and its depth, assuming a mean velocity model up to the focal depth, is well constrained by the modelling of Tavera (1991). The modelling of this earthquake with a spherical earth model (Červený and Janský, 1983) is obtained for a thrust mechanism with a small strike-slip component (azimuth 245°, dip 63°, slip 100°), consistent with the Tavera study (1991). The source duration is 4 s. Synthetic and observed seismograms (Fig. 13) show good agreement at all the stations, except for AGD (azimuth 151°), RER (azimuth 153°) and HYB (azimuth 105°); at these three stations the observed amplitude for the pP phase is higher.
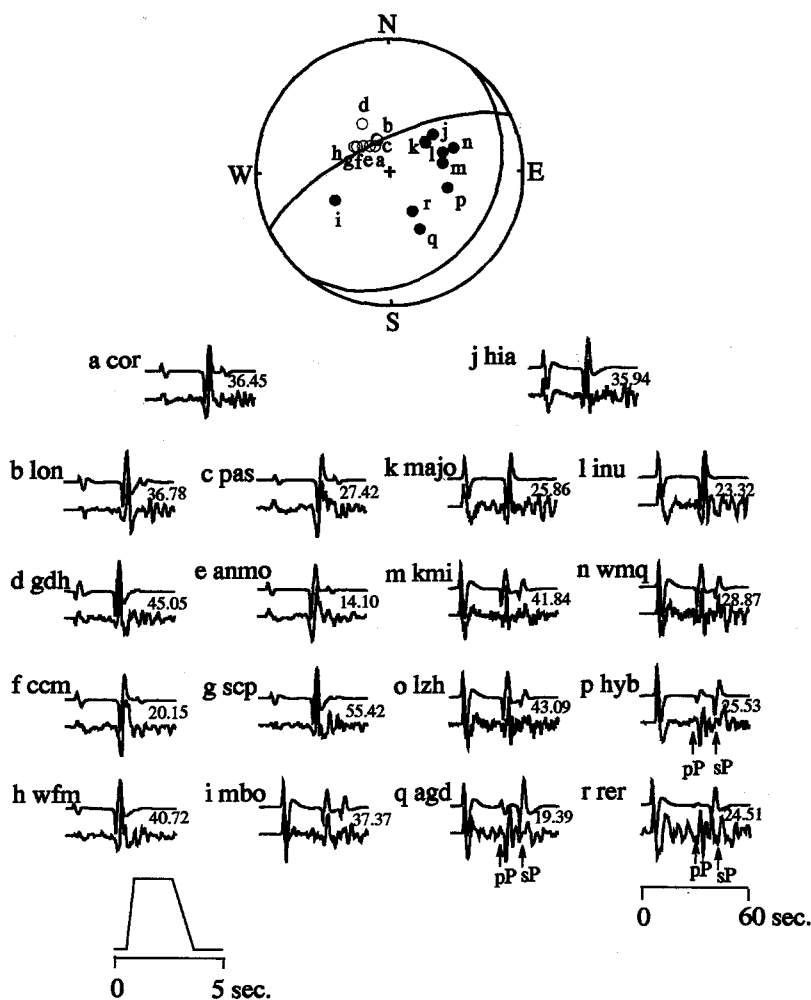

Fig. 13. Modelling with a symmetrical spherical Earth model of the 1990 Vrancea earthquake. The synthetic seismogram is shown above the observed seismogram. The number on the left is the epicentral distance and the right one is the moment at the station. The source is trapezoidal and 4 s long. The thrust mechanism has a strike of 245°, a dip of 63° and a slip of 100°. The take-off angles of the direct P wave are represented on the focal sphere. Three stations (AGD, RER and HYB) present anomalies in the amplitude of the pP and sP phases, which are reflections at the free surface.

The sP synthetic phase shows a large amplitude only for AGD, whereas the others show good agreement with the synthetic amplitude calculated with a spherical model. Nevertheless, all the sP phases arrived too early in the synthetic seismograms at these three stations. The take-off angles of the pP phase, especially for AGD, are located near the nodal plane, providing a very low amplitude, as shown in Fig. 14. As this mechanism is very well constrained by 15 stations (Fig. 13), and the SH waves as shown by Tavera (1991), we believe that the anomalous amplitudes for the pP and sP synthetic phases are caused by the structure around the source changing the take-off angles of the reflected phases.

Seismic activity in the Vrancea region has been attributed to the presence of a palaeo-subduction zone (Onescu, 1986; Tavera, 1991), and indicates a Benioff zone, as shown in Fig. 15. Nevertheless, a model of the subduction zone with the source located at 90 km depth did not improve the modelling of seismograms of AGD, RER and HYB. The effect of the curvature of the slab did not provide a large amplitude for the pP phases which pass through the slab. This leads us to suppose that the problem is more superficial and

due to near-surface structures. The Carpathian arc, in which the Vrancea region is located, is surrounded by the Transylvanian and Pannonian basins to the west and by the Moesian basin to the east. These sedimentary basins are wide and their depth might be greater than 10 km in the area (Radulescu and Sandulescu, 1974).

4.1. Modelling of the 30 May 1990 earthquake

The introduction of sedimentary layers allows us to achieve a better fit of the observed seismograms (Fig. 16(b)). Structures defined by rays are described in Fig. 17(a). To fit the large amplitude of the observed pP phase, an interface dipping at 20° to the east separating a sedimentary layer with a constant velocity of 4.6 km s^{-1} and a granitic layer with a velocity of 6.5 km s^{-1} provides a shift of the take-off angles in the higher amplitude of the focal sphere accompanying by large amplitudes in the Green function (Fig. 17(b)). Problems remain in amplitude for the pP phase on the synthetic seismogram at AGD and RER. The interface dipping at 20° seems to be an average, which corresponds to a synthetic amplitude consistent with the observed signal for HYB,
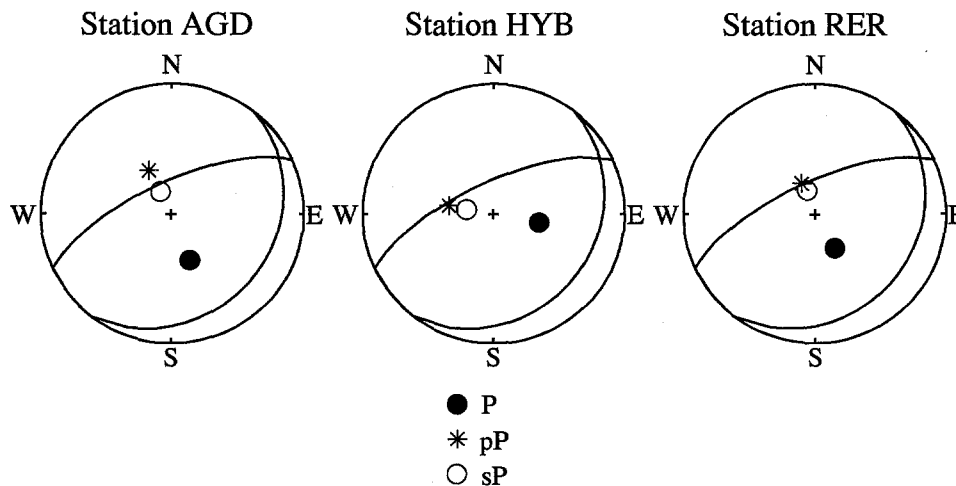

Fig. 14. The thrust mechanism of the modelling shown in Fig. 13, on an equal area projection of the focal sphere. The take-off angle of the reflected phase for AGD at 36.9° receiver distance, HYB at 51.4° and RER at 71.7° are plotted and obtained from the modelling in Fig. 13. The sP phase has a more vertical angle than the pP phase, in a higher-amplitude region of the radiation pattern.
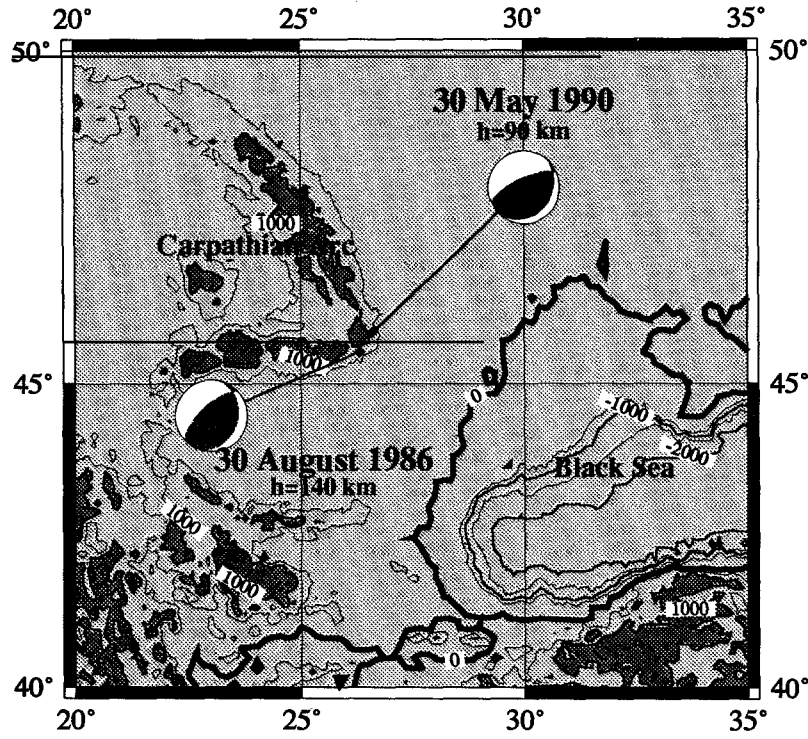
a.
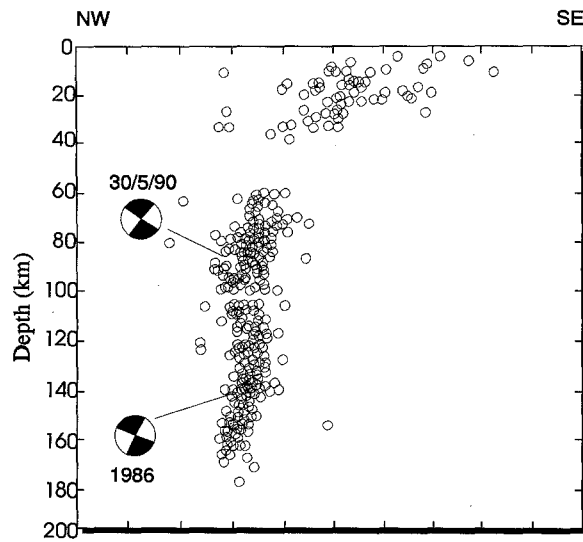
b.

Fig. 15. Seismic map of the Vrancea region, from Tavera (1991). (a) Map of the Vrancea region with the epicentres of the 30 May 1990 and 30 August 1990 earthquakes. (b) Distribution in depth of seismic activity, on a SW–NE profile. A Benioff plane is suggested by the seismicity, with a dip of 60° between 60 and 100 km depth and a dip of 70° between 120 and 180 km depth.

Station AGD   **Station HYB**   **Station RER**

● P
* pP
○ sP,sd1P
△ pd1P,pd2P

a.

agd 36.9 ... 12.68

hyb 51.4 ... 13.59

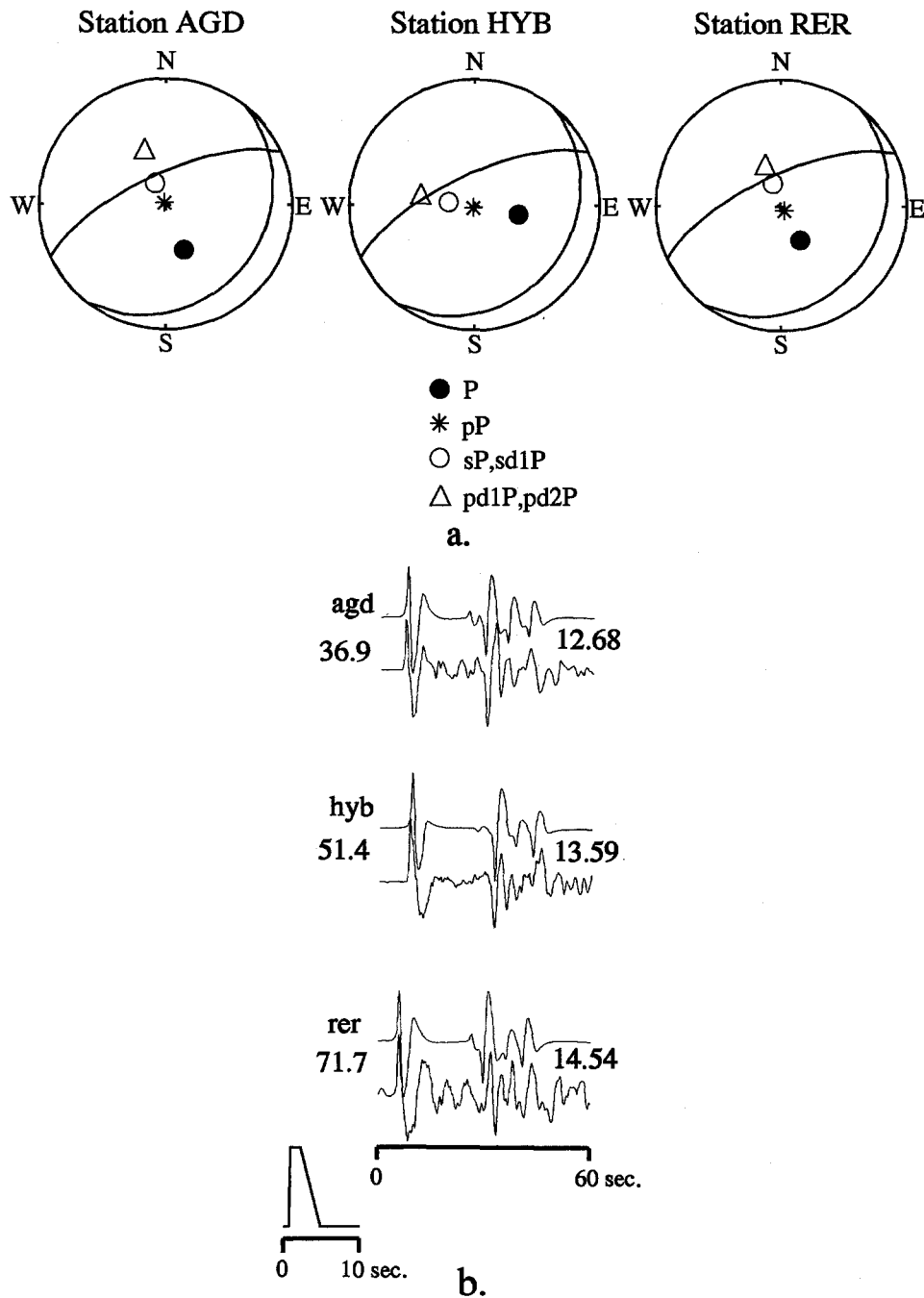rer 71.7 ... 14.54

0   60 sec.

0   10 sec.   **b.**

Fig. 16. (a) As in Fig. 14, but with the take-off angle calculated in the complex media. The take-off angles of the pP phase have been shifted to higher amplitude near the direct P wave. As the take-off angle of the sd1P phase is the same as that of the sP phase, these phases are represented by the same symbol; the pd1P and pd2P phases are also shown by one symbol. (b) Synthetic seismograms for AGD, RER and HYB obtained with the hybrid method for the same thrust mechanism as in Fig. 13. The number on the right is the epicentral distance in degrees, and that on the left is the moment of each station. The source is still trapezoidal but it exceeds 3 s. We fit the amplitude of the sP phase. The amplitude of the pP phase is not totally recovered for AGD and is too large for RER, but the amplitude of these phases has been improved compared with the spherical model. Many reflections have been added in the synthetic waveform.

but provides a higher synthetic amplitude at RER, and a lower one for AGD. As HYB is not on the same azimuth (105°) as AGD and RER (150°), this model seems to be suitable on the azimuth of HYB. Propagation in 2D media allows us to

describe the apparent dip of the interface, but not the true one.

The sP phase has no amplitude when it passes through the dipping interface. This is why the sP phase follows a classical ray tracing with a plane
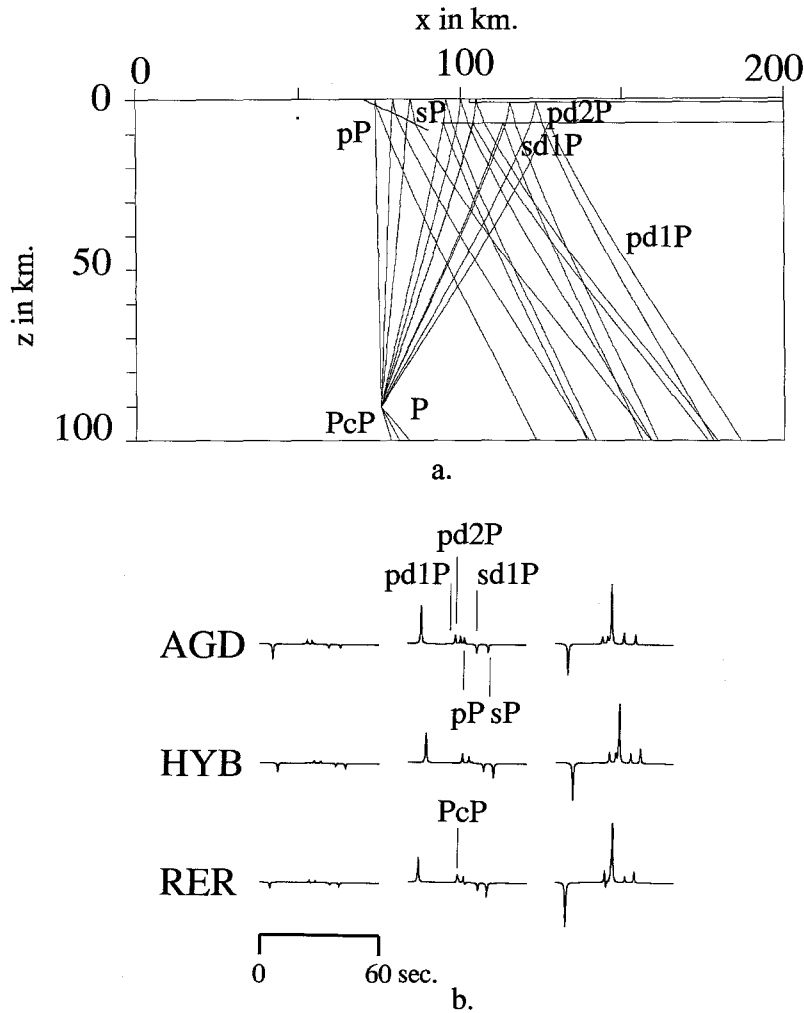

Fig. 17. (a) Ray tracing in the 2D cartesian model around a source located at 90 km depth. The 20° dipping interface delimits a sedimentary layer with a constant velocity of 4.6 km s⁻¹ for the P wave allowed a vertical take-off angle. The interface at 7 km is the bottom of a sedimentary basin with a constant velocity of 4.4 km s⁻¹ for the P wave. It induces reflection at the bottom, the sd1P and pd1P phases. Another sedimentary layer of 1 km depth and with a constant velocity of 2.5 km s⁻¹ induces reflection at its bottom, the pd2P phase. The reflections at the free surface, the sP phases, cross the thick basin for RER and HYB, and for AGD they also cross the thin basin. Only interfaces detected by the rays are plotted. (b) Green functions from ray theory for AGD at 36.9° receiver distance, HYB at 51.4° and RER at 71.7°. The six reflection phases described in (a) are present in these Green functions. The reflection at the external core, PcP, is present in the Green function of RER. (Note the large amplitude of the pP phase at the three stations, owing to an increasing reflection coefficient.)

interface in the 2D cartesian model we used, describing a sedimentary basin of 7 km depth to the west of the dipping interface, which is necessary to fit the sP phase in time. For the amplitude of the sP phase at AGD, another sedimentary layer of 1 km depth with a velocity of 2.5 km s^{-1} for the P wave below the surface was necessary to fit the lower amplitude of the observed sP phase.

The contrast of velocity between the deep sed-

imentary basin and the granitic layer induces supplementary reflections at the bottom of the sedimentary layer: the sd1P and the pd1P phases. The pd1P phase arrives 5 s before the pP phase on synthetic seismograms, and has a low amplitude. The sd1P phase constrains the depth and velocity of the basin because it provides a large amplitude arriving between the pP and sP phases, consistent with the observed one. Another reflec-
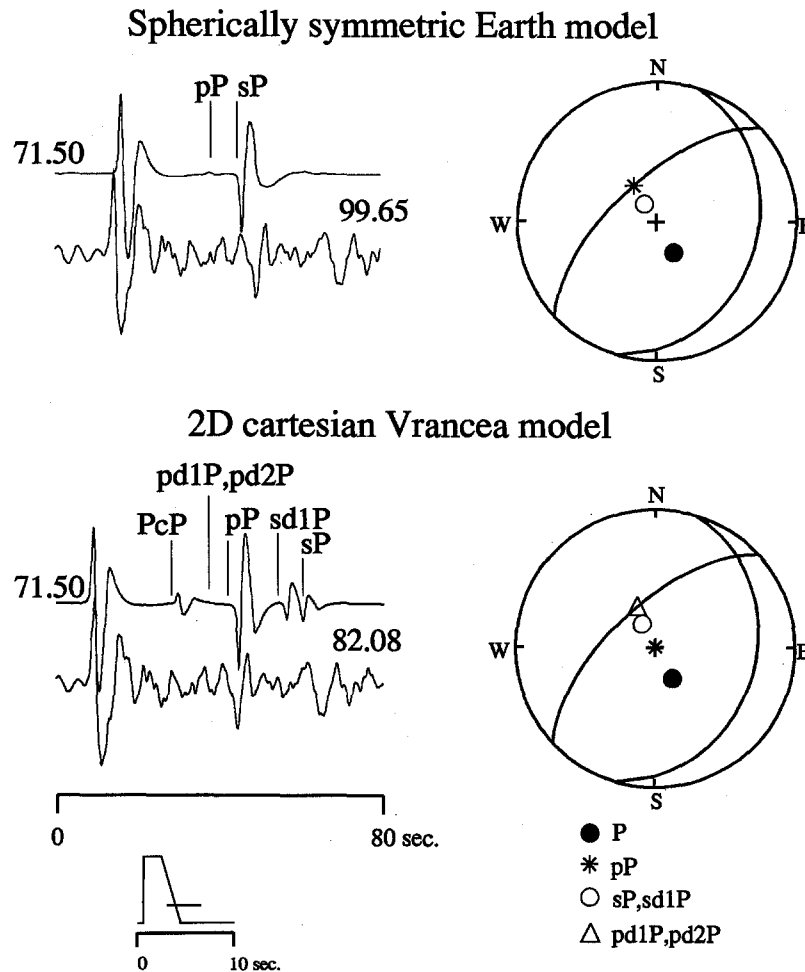

Fig. 18. Modelling of the 30 August 1986 event with a spherical Earth model and with the 2D deduced model for the Vrancea region. Phases are marked on synthetic seismograms, above, and the observed seismograms are shown below. The take-off angle of each phase is located on the focal sphere. The observed seismogram shows a large amplitude for the pP phase which is not present in modelling with the Earth model, and the pP and sP phases show a strong delay. The modelling with the 2D deduced model gives a better fit in time and in amplitude for the pP phase, but the sP phase is still delayed. (Note the shift of the take-off angle of the pP phase.)

tion is possible at the bottom of the low-velocity sedimentary basin, the pd2P phase. This phase has a low amplitude on the Green function and its take-off angle is the same as that of the pd1P phase; it provides a very low amplitude on the synthetic seismograms, but is significant at AGD just before the pP phase.

The synthetic PcP phase, a reflection from the external core, shows an amplitude at RER 5 s before the pP phase. This amplitude is not easy to fit to the observed seismograms, which show large period phases between the P and pP phases, probably owing to local reverberation. The same feature is present at AGD. A phase between the sd1P and sP phases is present with a high amplitude at HYB and RER. We tested for double reflection at the dipping interface, but this test was unsuccessful as the phases cannot be transmitted through the dipping interface; we also tested for double reflection in the low-velocity basin, but this gave an amplitude that was too low.

We deduced a hypothetical model to fit the observed seismograms at these three stations. This model is still not perfect, but improves the modelling compared with the spherical model. We choose to represent only interfaces indicated by rays, but the dipping interface seems to be connected with the sedimentary basin on the east. Koch (1985) has deduced by nonlinear inversion of the local seismic travel-time in the Vrancea region a 3D model of velocity. This model provides evidence for a sedimentary layer basin whose interface dips towards the east. The velocity are greater than for our model below 4 km depth. For structural aspects, Ellouz et al. (1994) has presented a geodynamic model of the Vrancea region. His model of structures presents a décollement level of 20° towards the east, separating the crystalline basement from the sedimentary layer in a minor Plio-Quaternary shortening event, but this interface is not continued to the surface as we have modelled.

We have checked the deduced Vrancea model on the RER station, the only station in this range of azimuth for an earthquake that occurred on 30 August 1986. In Fig. 18 is shown the modelling for this event with a spherically symmetric Earth model and with the 2D cartesian deduced model. The modelling for RER with a spherical Earth model shows the same anomalies: large sP phase and low amplitude of the pP phase, with a strong delay of these phases. The modelling with the already deduced model did not provide a good fit: the fit in time and the recovery of the pP phase amplitude are convincing, but a lower delay is still present for the sP phase. We might improve our model to fit this sP phase. Without any other stations, this exercise is not very significant. One possible interpretation is a low-viscosity zone postulated by Fuchs et al.(1979) between 90 and 140 km; the depth of this event is 140 km. Another possible interpretation is a 3D model. As this event is 20 km away from the 30 May 1990 event (Fig. 15(a)), we may have a 3D effect of azimuthal distortion on the focal sphere, which could decrease the synthetic amplitude obtained with the 2D cartesian model.

5. Conclusion

Structures around the source affect significantly the propagation of seismic waves. We have constructed a tool to handle complex propagation for a 2D model with lateral variations in velocity as well as with arbitrary shapes of interfaces. We have found that non-flat structures from a dipping seafloor to a curved slab modify seismic waveforms. We call the global effect of a complex propagation and of the associated modification of the radiation pattern the azimuthal distortion of the focal sphere.

The 1990 Romanian earthquake records present anomalous amplitude for reflections at the free surface for three stations in a given range of azimuth. These signals are observed with new broadband instruments; each individual phase is identified on the seismogram, whereas, for a longer-period instrument, they arrive together. We fit this anomalous amplitude by adding at the surface other reflections at the bottom of a sedimentary basin. Although the presence of two actual sedimentary basins justifies our hypothesis, the model is hypothetical, as we have only three stations in this range of azimuth. To constrain

our model further, we need information on the local structure with geophysical data such as seismic profiles or local records.

With information on the local structure, we are able to resolve the source parameters of an earthquake in greater detail. For shallower events than the Romanian earthquake, multiple reflections would not be so well separated. A more precise knowledge of the upper crust is required for a better analysis of focal mechanisms and source processes, and, consequently, for a deeper understanding of the associated tectonics.

Acknowledgements

References

Aki, K. and Richards, P., 1980. Quantitative Seismology: Theory and Methods. W.H. Freeman, San Francisco, Vol. I, 932 pp.; Vol. II, 557 pp.

Burridge, R., 1976. Some Mathematical Topics in Seismology. Courant Institute of Mathematical Sciences, New York University, Vol. I, 123 pp.; Vol. II, 317 pp.

Červený, V., 1985. The application of ray tracing to the numerical modelling of seismic wave fields in complex structures. In: Handbook of Geophysical Exploration, Section 1, Seismic Exploration, Vol. 15A. Geophysical Press, pp. 1–119.

Červený, V. and Janský, J., 1983. Ray amplitude of seismic body waves in homogeneous radially symmetric media. Stud. Geophys. Geod., 27; 9–18.

Chapman, C.H., 1985. Ray theory and its extension: WKBJ and Maslov seismograms. J. Geophys., 58: 27–43.

Chapman, C.H., 1987. The Radon transform and seismic tomography. In: G. Nolet (Editor), Tomography in Seismology and Exploration Seismics. D. Reidel, Dordrecht, pp. 25–47.

Dziewonski, A.M. and Anderson, D.L., 1981. Preliminary reference earth model. Phys. Earth Planet. Inter., 25: 297–356.

Ellouz, N., Roure, F., Sandulescu, M. and Badescu, D., 1994. Balanced cross section in the eastern Carparthians (Romania): a tool to quantify Neogene dynamics. In: Geology Evolution of Sedimentary Basin, Congress of Moscow, submitted.

Farra, V., Virieux, J. and Madariaga, R., 1989. Ray perturbation theory for interfaces. Geophys. J. Int., 99: 377–390.

Farra, V. and Madariaga, R., 1987. Seismic waveform modeling in heterogeneous media by perturbation theory. J. Geophys. Res., 92: 2697–2712.

Fuchs, K., Bonjer, K-P., Bock, G., Cornea, I., Radu, C., Enescu, D., Jianu, D., Nourescu, A., Merkler, G., Moldoveanu, T., and Tudorache, G., 1979. The Roumanian earthquake of March 4, 1977. Tectonophysics, 53: 225–247.

Kendall, J.M. and Thomson, C.J., 1993. Seismic modelling of subduction zones with inhomogeneity and anisotropy—I. Teleseimic P waveform tracking. Geophys. J. Int., 112: 39–66.

Koch, M., 1985. Nonlinear inversion of local seismic travel time for simultaneous determination of the 3D-velocity structure and hypocentres—application to the seismic zone Vrancea. J. Geophys., 56: 160–173.

Lambaré, G., Virieux, J., Madariaga, R. and Side, J., 1992. Iterative asymptotic inversion in the acoustic approximation. Geophysics, 57: 1138–1154.

Langston, C.A. and Helmberger, D.V., 1975. A procedure for modelling shallow dislocation sources. Geophys. J.R. Astron. Soc., 42: 117–130.

Madariaga, R. and Papadimitriou, P., 1985. Gaussian beam modelling of upper mantle phases. Ann. Geophys., 3: 799–812.

Monfret, T., Deschamps, A. and Romanowicz, B., 1990. The Romanian earthquakes of August 30, 1986 a study based on GEOSCOPE, very long period and broad-band data. Pageoph., 133: 367–379.

Müller, G., 1971. Approximate treatment of elastic body waves in media with spherical symmetry. Geophys. J.R. Astron. Soc., 23: 435–449.

Okamoto, T. and Miyatake, T., 1989. Effects of near source seafloor topography on long-period teleseismic P waveforms. Geophys. Res. Lett., 16: 1309–1312.

Onescu, M.C., 1986. Some source and medium properties of the Vrancea region, Romania. Tectonophysics, 126: 245–258.

Radulescu, D. and Sandulescu, M., 1974. The plate-tectonics concept and geological structure of the Carpathians. Tectonophysics, 16: 155–161.

Tavera J., 1991. Etudes des mécanismes focaux de gros séismes et sismicité dans la région de Vrancea—Roumanie. Rapport de stage de DEA de geophysique interne, Institut de Physique du Globe, Paris, 45 pp.

Virieux, J. and Farra, V., 1991. Ray tracing in 3-D complex isotropic media: an analysis of the problem. Geophysics, 16: 2057–2069.

Virieux, J., Farra, V. and Madariaga, R., 1988. Ray tracing for earthquake location in laterally heterogeneous media. J. Geophys. Res., 93: 6585–6599.

Wiens, D.A., 1987. Effects of near source bathymetry on teleseimic P waveforms. Geophys. Res. Lett., 14: 761–764.

Wiens, D.A., 1989. Bathymetric effects on body waveforms from shallow subduction zone earthquakes and application to seismic processes in the Kurile trench. J. Geophys. Res., 94: 2955–2972.